Low-Temperature Thermopower in CoSbS

Qianheng Du (杜乾衡),[1,2,†] Milinda Abeykoon,[3] Yu Liu (刘育),[1] G. Kotliar,[1,4] and C. Petrovic[1,2,*]

[1]*Condensed Matter Physics and Materials Science Department, Brookhaven National Laboratory, Upton, New York 11973, USA*
[2]*Department of Materials Science and Chemical Engineering, Stony Brook University, Stony Brook, New York 11790, USA*
[3]*Photon Science Division, National Synchrotron Light Source II, Brookhaven National Laboratory, Upton, New York 11973, USA*
[4]*Department of Physics and Astronomy, Rutgers University, Piscataway, New Jersey 08856, USA*

We report on giant thermopower of $S = 2.5$ mV/K in CoSbS single crystals: a material that shows strong high-temperature thermoelectric performance when doped with Ni or Se. Changes of low-temperature thermopower induced by a magnetic field point to the mechanism of electronic diffusion of carriers in the heavy valence band. Intrinsic magnetic susceptibility is consistent with the Kondo-insulatorlike accumulation of electronic states around the gap edges. This suggests that giant thermopower stems from temperature-dependent renormalization of the noninteracting bands and buildup of the electronic correlations on cooling.

Thermoelectric materials convert heat into electric power and vice versa, which is attractive for power generation and greenhouse gas emissions reduction [1]. Even though efficient thermoelectrics are also needed for applications below room temperature, progress in cryo-thermoelectric materials discovery has been modest [2]. In a cryogenic environment, there are two major differences when compared to high-temperature automotive or solar applications. Because the temperatures of interest are small, for a high figure of merit $ZT = (S^2\sigma/\kappa)T$, where S is thermopower and σ and κ are electrical and thermal conductivities, the thermoelectric power factor $(S^2\sigma)$ must be large. In addition, electronic correlations cannot be neglected [3,4]. Therefore, FeSb$_2$-like electronic systems [5,6] with the largest thermopower and thermoelectric power factors known to date [7,8] could be essential materials for future thermoelectric cryodevices.

The thermopower of FeSb$_2$ reaches colossal values of up to -45 mV/K [7]; however, the physical mechanism is not well understood. From the Mott formula, $S = -[(\pi k_B)^2/3e]T(\partial \ln\sigma/\partial E)|_{E_F}$, and so values on the order of $S \approx -[(\pi^2 k_B)/3e][T/T_F] \approx 10$ μV/K are to be expected for the diffusion mechanism in metals where states at the Fermi level take part in the conduction process [9]. In semiconductors, the electronic contribution to thermopower scales with the distance from the Fermi level in units of $k_B T$ and with its fractional contribution to the total current. Therefore, semiconductors have typically larger diffusion thermopower when compared to metals; however, commonly observed values are still in the hundreds of microvolts per kelvin range [10]. Whereas there are arguments against the phonon drag in FeSb$_2$ [11,12], recent studies suggest nearly ballistic phonons dragging massive electrons to enhance thermopower up to $|S| = 27$ mV/K in high-purity

FeSb$_2$ single crystals [13]. In order to make progress and enable predictive materials design, it is important to discover new materials with high thermoelectric parameters and with tunable physical properties.

Ternary crystal structures offer higher tunability when compared to binary compounds such as marcasite FeSb$_2$ [14]. Recently, it was shown that CoSbS [15] could be a high-temperature thermoelectric material due to several positive factors that work simultaneously to enhance its thermoelectric performance [16]. Combined linearized augmented plane wave theoretical and experimental studies confirmed this to be the case, unveiling additional features in the electronic structure such as substantial band degeneracy near edges, flat dispersions throughout the entire Brillouin zone, and a large density of states rising rapidly around the gap [17]. Co$_{1-x}$Ni$_x$SbS and CoSbS$_{1-x}$X$_x$ ($X =$ Se, Te) showed a figure of merit $ZT = (0.5-0.62)$ in the (730–900) K range and a high power factor [18–20]. Moreover, even higher values of $ZT > 1$ at 600 K have been predicted by density functional theory in optimized CoSbS-based materials [21].

Here, we unveil the low-temperature thermoelectric properties of CoSbS and report $S = 2.5$ mV/K at 40 K. In contrast to FeSb$_2$, where the mechanism of colossal S is still controversial, we show that such large values can be explained by the electronic diffusion in the heavy valence band. Our results imply a Kondo-insulatorlike scenario of the electronic correlations buildup associated with the thermopower peak; the intrinsic magnetic susceptibility can be understood within a model of metallic spin paramagnetism, albeit with a large low-temperature renormalization of the noninteracting bands [22,23].

Single crystals of CoSbS were grown by heating starting materials first at 500 °C for 6 h and then to 1000 °C. Crystals
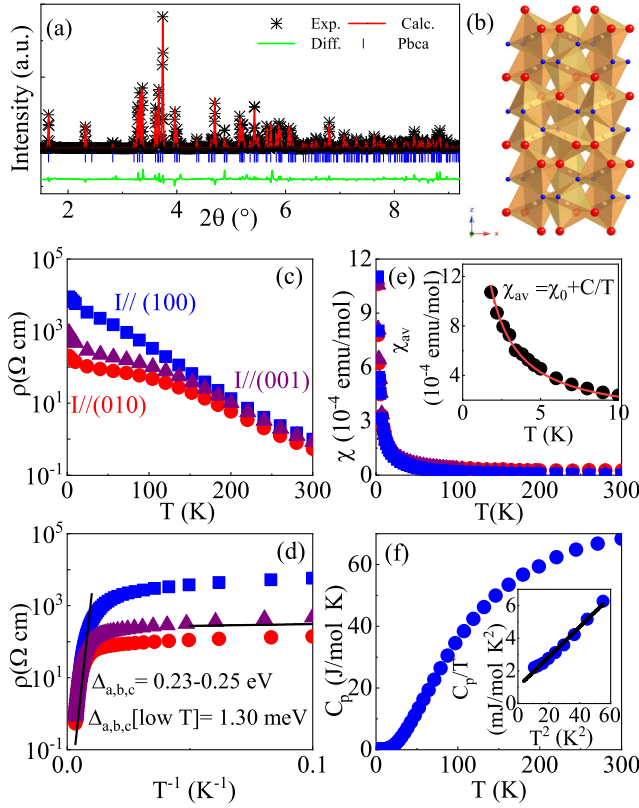
FIG. 1. (a) Powder XRD pattern and refinement. Data are shown by +, and fitting and difference curves are given by red and green solid lines, respectively. (b) Crystal structure of CoSbS. (c) and (d) Resistivity vs temperature for CoSbS crystals with current along different crystalline axes, revealing semiconductor behavior with different temperature regions of activated transport. (e) Anisotropic magnetic susceptibility vs temperature for a CoSbS crystal in a magnetic field of 1 T. Inset shows average magnetization. (f) Heat capacity for CoSbS crystals; inset shows low-temperature region.

were decanted at $650\,^\circ\mathrm{C}$ after the slow-cooling process. They were oriented and polished along principal crystallographic axes for four-probe resistivity and thermal transport measurements. Magnetic, transport, and thermal measurements were carried out in Quantum Design PPMS-9 and MPMS-5XL. In thermoelectric measurement, the magnetic field is applied along the b axis, whereas the temperature gradient is along the a axis. Synchrotron powder x-ray diffraction (XRD) data were taken at NSLS2 beamline 28-ID-1.

The powder x-ray diffraction pattern confirms that single crystals crystallize in a $Pbca$ space group with refined lattice parameters $a = 0.58357(1)$ nm, $b = 0.59499(1)$ nm, and $c = 1.16563(2)$ nm [Fig. 1(a)] [15]. The space group is similar to pyrite and marcasite, where each cation is octahedrally coordinated with six nearest neighbor anions [Fig. 1(b)]. In CoSbS, each octahedron shares an edge with one neighboring octahedron and corners with ten additional neighboring octahedra. The element analysis performed

using an energy-dispersive x-ray spectroscopy in a JEOL LSM-6500 scanning electron microscope indicated CoSbS composition.

Temperature-dependent resistivity is rather anisotropic [Figs. 1(c)–1(d)]; $\rho_c \gg \rho_{a,b}$ at low temperature. There is a similar activated behavior in the temperature of $\rho = \rho_0 \exp(\Delta/2k_B T)$ over limited temperature ranges. The activated behavior in the $200 < T < 300$ K range gives $\Delta = 0.23$–$0.25(1)$ eV. At low temperatures of $10\,\mathrm{K} < T < 20$ K, we detect an additional small gap of $\Delta_{\mathrm{low}T} = 1.30(1)$ eV. Temperature dependence of the resistivity is consistent with a lightly doped semiconductor: impurity-band conduction with a 1.30 meV gap dominates at low T, and intrinsic conduction with $\Delta = 0.24(2)$ eV dominates at high T [24].

CoSbS shows paramagnetic magnetic susceptibility [Fig. 1(e)], which is consistent with the low spin state of Co^{3+} [25]. Whereas the anistropy in the $\rho(T)$ is significant, $\chi(T)$ shows much less anisotropy. The low-temperature tail could come from paramagnetic impurity effects, i.e., some residual imperfections and off-stoichiometry similar to FeSi and FeSb$_2$ [5,26]. We fit the average low-temperature magnetization $\chi_{\mathrm{av}} = \frac{1}{3}(\chi_a + \chi_b + \chi_c)$ [5] using Curie law $\chi = \chi_0 + c/T$ [Fig. 1(e) inset] to obtain the Curie constant associated with spin of $3/2$ Co^{2+}. The fraction of Co^{2+} is 1.6%. The intrinsic impurity-free magnetic susceptibility of CoSbS will be discussed later. The heat capacity of CoSbS crystals [Fig. 1(f)] shows the electronic specific-heat coefficient γ from $C/T = \beta T^2 + \gamma$ is $\gamma(T \to 0) \approx 1.4(1) \times 10^{-3}$ J/mol K^2, as expected for a semiconductor. The Debye temperature is 426(2) K, which implies an average sound velocity of $\nu_s \approx 3700$ m/s [27].

Hall resistivity ρ_{xy} in a magnetic field [Figs. 2(a) and 2(b)] is not linear, confirming the presence of multiband electronic transport [17]. In a two-carrier system, the Hall coefficient is

$$R_H = \rho_{xy}/H = \rho_0(\alpha_2 + \beta_2 H^2)/(1 + \beta_3 H^2),$$

where $\alpha_2 = f_1\mu_1 + f_2\mu_2$; $\beta_2 = (f_1\mu_2 + f_2\mu_1)\mu_1\mu_2$; and $\beta_3 = (f_1\mu_2 + f_2\mu_1)^2$, where $\rho_0 = \rho(\mu_0 H = 0)$;

$$f_i = \frac{|n_i\mu_i|}{\Sigma|n_i\mu_i|}$$

is the f factor; and n_i and μ_i are individual carrier band concentrations and mobilities [28]. From the model, we obtain both carrier band concentrations and mobilities [Figs. 2(c) and 2(d)]. Different from the conventional electrons or holes that are associated with a continuous energy band, "carrier" denotes a set of carriers with identical mobility corresponding to only one energy and/ or one degenerate energy level in the model. Carriers in the low mobility band are denoted as carrier 1 and, in the high mobility band, are denoted as carrier 2. In the
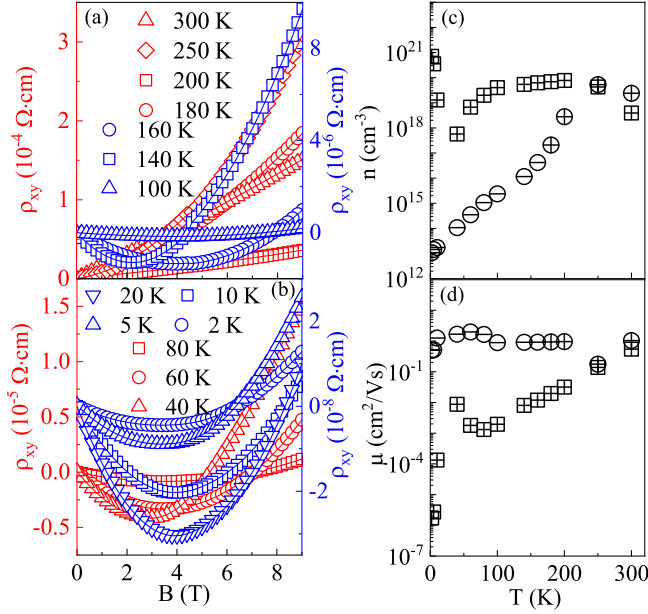
FIG. 2. (a) and (b) Hall resistivity (ρ_{xy}) vs magnetic field at different temperatures with current along the a axis. Solid lines are fits using the two-band model. (c) Carrier concentration and (d) Hall mobility as functions of temperature. $+$ denotes the hole carriers, and $-$denotes the electron carriers. Squares represent carrier 1 and circles represent carrier 2, as delineated in the text.

high-temperature range where the intrinsic conduction dominates ($T > 180$ K), both carrier 1 and carrier 2 are holelike; whereas in the temperature range where extrinsic conduction dominates, carrier 1 is holelike and carrier 2 is electronlike. At 300 K, the concentration of carrier 2 ($n_2 \sim 10^{19}$ cm^{-3}) is about one order of magnitude larger than carrier 1 ($n_1 \sim 10^{18}$ cm^{-3}). Room-temperature carrier concentration values are similar to the values observed in narrow-gap Kondo semiconductors FeGa$_3$ and Ce$_3$Bi$_4$Pt$_3$ [29,30]. There is a sharp decrease of the carrier 2 concentration below 200 K to $n_2 \sim 10^{13}$ at 2 K. At the same time, the n_1 increases by about one order of magnitude, keeping the total carrier concentration unchanged. Another difference between the two carrier types is in the Hall mobility. The mobility of carrier 2 (μ_2) is one to several orders larger than the mobility of carrier 1 (μ_1) below 250 K. Above 200 K, the intrinsic conduction dominates and the conduction of the accepter band occurs with low mobility. Carrier 2 comes from the intrinsic carriers and extrinsic carriers in the valence band, and carrier 1 is the extrinsic carrier in the impurity band. The crossover of n_1 and n_2 could possibly be explained by the freezing of extrinsic carriers into the accepter band about 0.5 meV above the valence-band edge [Figs. 1(c) and 1(d)].

Thermopower $S(T)$ shows a peak at 40 K [Fig. 3(a)]; its sign is consistent with low-temperature Hall data below 300 K, and the curve is very similar to that of FeSb$_2$ crystals [7,13]. Having in mind the dominant carrier type in the

temperature region of thermopower enhancement, we consider the single-degenerate parabolic band [11,31]:

$$S(T) = \pm \frac{\pi^2}{3} \frac{k_B}{e} \frac{k_B T}{\epsilon_F} \left(r + \frac{3}{2} \right). \quad (1)$$

Within the free-electron approximation, the Fermi energy ϵ_F is $\epsilon_F = h^2/2m^\star (3n/8\pi)^{2/3}$, whereas $m^\star = m_0$, where m_0 is the free-electron mass, and n could be estimated from the Hall effect. The carrier scattering parameter is usually between -0.5 and 1.5. Here, it is assumed to be $-\frac{1}{2}$; however, fit results do not critically depend on the r value. Notably, to describe the observed peak in $S(T)$, an enhancement factor of 6.5 in the $m^\star$ from the free-electron mass is required. This points to the strong electronic correlations and a relatively heavy valence band. The fitted line is shown in Fig. 3(a) as a green solid line. We can exclude the phase transition contribution to thermopower because CoSbS shows neither a metal insulator [Fig. 1(c)] nor a crystal structure change [Fig. 3(b)] at 40 K. The thermopower peak arising from the spin-fluctuation mechanism in semiconductors occurs at temperatures of the long-range or the short-range magnetic order [32,33]. Because CoSbS does not show any magnetic order, the spin-fluctuation mechanism of thermopower enhancement is unlikely.

The lattice thermal conductivity is usually treated using a Debye approximation [34]:

$$K_L = \frac{k_B}{2\pi^2 \nu_s} \left(\frac{k_B}{\hbar} \right)^3 T^3 \int_0^{\theta_D/T} \frac{\tau_c x^4 e^x}{(e^x - 1)^2} dx, \quad (2)$$

where $x = \hbar\omega/k_B T$ is dimensionless, ω is the phonon frequency, k_B is the Boltzmann constant, $\hbar$ is the Plank constant, θ_D is the Debye temperature, ν_s is the velocity of sound, and τ_c is the relaxation time. The overall relaxation rate τ_c^{-1} can be determined by combining different scattering processes

$$\tau_c^{-1} = \tau_B^{-1} + \tau_D^{-1} + \tau_U^{-1}$$
$$= \frac{\nu}{L} + A\omega^4 + B\omega^2 T e^{-\theta_D/T}, \quad (3)$$

where τ_B, τ_D, and τ_U are the relaxation times for boundary scattering, defect scattering, and Umklapp processes, respectively. The adopted values of the parameters are $A = 3.0 \times 10^{-43}$ s^3 and $B = 6.2 \times 10^{-18}$ s K^{-1}, and the phonon mean free path at low temperature in the boundary scattering regime is $L = 6.6 \times 10^{-5}$ m. It should be noted [inset (a2) in Fig. 3(a)] that $\kappa(T)$ values are smaller when compared to FeSb$_2$, which is probably due to the enhanced defect and Umklapp scattering processes of high-momentum phonons [7].

Next, we discuss the mechanism of giant thermopower in detail. It is instructive to evaluate the contribution of the
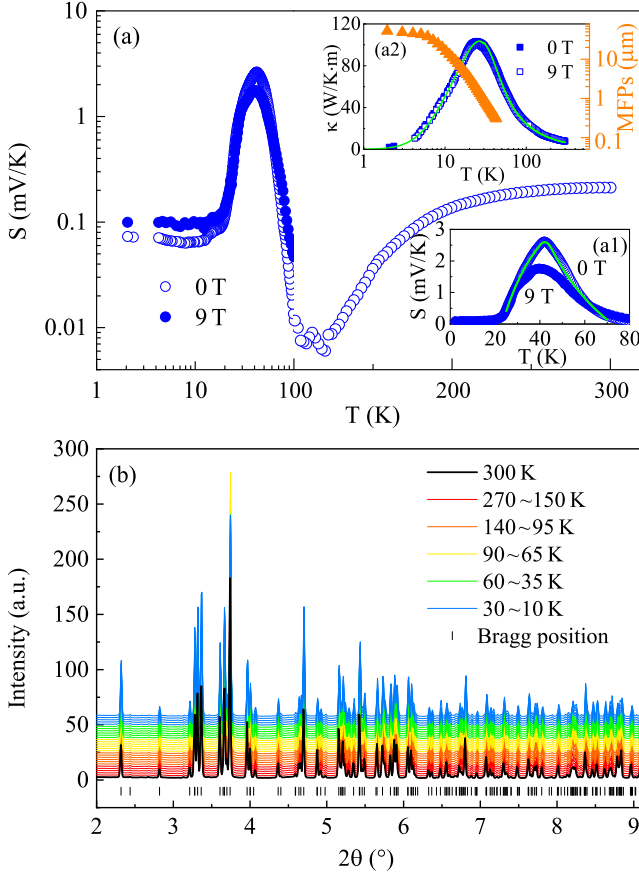
FIG. 3.   (a) Thermopower of CoSbS crystal with the temperature gradient along (100) measured below 300 K. (b) Powder XRD patterns from room temperature to 10 K taken in 10 K steps below 90 K and 30 K steps above 90 K. There are no new reflections in the temperature range of thermopower rise, indicating the absence of the structural transition. Insets: (a1) low-temperature thermopower and fit using single-band model (see text), and (a2) thermal conductivity for the same crystal and the corresponding phonon mean free path (MFP). Green line shows fitting of thermal conductivity.

phonon drag. First, we note that the electronic contribution to $\kappa(T)$ using the Wiedemann-Franz law is negligible; i.e., the phonon $\kappa_P(T)$ and total $\kappa(T)$ are indistinguishable. The phonon-drag thermopower is directly related to the phonon mean free path l_p by $S_{ph} = \beta \nu_s l_p / \mu T$ [35,36], where the β parameter describes the relative interaction strength of the electron (or hole) and phonon with $0 < \beta < 1$, and μ is the mobility of the hole in the valence band. Because $\kappa = C_\nu \nu_s l_p / 3$ [37], we estimate the phonon mean free path l_p to be about 0.7 μm at the maximum thermopower and 53 μm at 2 K [Fig. 3(a) inset (a2)], which is consistent with the Callaway model. This is several orders of magnitude smaller when compared to not only FeSb$_2$ but also to typical materials with a phonon-drag thermopower mechanism, such as Ge [11,38]. Together with the observation that $S(T)$ and $\kappa(T)$ are maximized at different temperatures [Fig. 3 insets (a1,a2)], present data strongly

suggest that the phonon-drag mechanism is not dominant in CoSbS. Furthermore, the maximum S value decreases from 2.5 mV/K in 0 T to 1.7 mV/K in 9 T [Fig. 3 inset (a1)]. This confirms the importance of electron diffusion in giant low-temperature thermopower in CoSbS, and it calls for the investigation of the m^* enhancement origin.

By subtracting impurity susceptibility from the measured $\chi(T)$, we obtain the intrinsic magnetic susceptibility [Fig. 4(a)]. There is a rise of paramagnetic spin susceptibility with temperature increase that can be explained with a narrow-band–small-gap model [22] with a pileup of states in the two narrow bands of width W, separated by an energy gap of $E_g = 2\Delta$ [inset in Fig. 4(a)]. This model has been successfully applied to point to Kondo-insulatorlike physics in correlated electron semiconductors FeSi and FeSb$_2$ [6,23].

The Pauli susceptibility of an itinerant electron system with $N(E)$ density of states is

$$\chi(T) = -2\mu_B^2 \int_{c\,band} N(E) \frac{\partial f(E,\mu,T)}{\partial E} dE, \qquad (4)$$

where μ_B is the Bohr magneton, and $f(E,\mu,T) = (\exp[(E-\mu)/k_BT]+1)^{-1}$. The factor of two in the equation is due to the holes in the valence band that contribute to χ in the same way as electrons in the conduction band. Taking $N(E) = Np/W$ and $\mu = W + \Delta$, where p is the number of states or cells and N is the number of unit cells, we obtain

$$\chi(T) = -2\mu_B^2 \frac{Np}{W} \frac{\exp(\beta\Delta)[1-\exp(\beta\Delta)]}{[1+\exp(\beta\Delta)]\{1+\exp[\beta(\Delta+W)]\}} + \chi_c. \qquad (5)$$

By fitting the magnetic susceptibility data [Fig. 4(a)], we obtain $W/k_B = 75$ K and $\Delta/k_B = 37$ K. Using the same
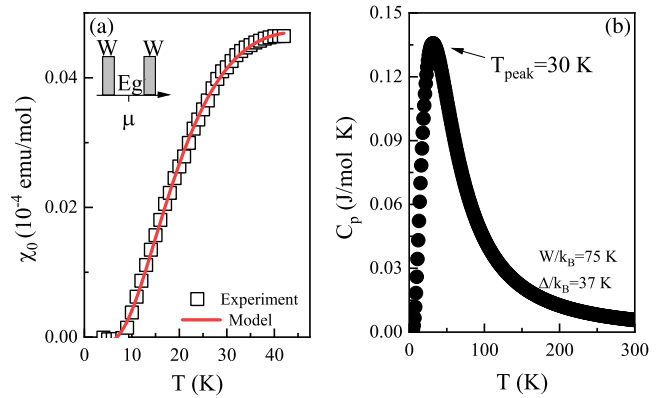

FIG. 4.   (a) Intrinsic low-temperature $\chi(T)$ obtained by subtraction of the Co^{2+} impurity Curie-Weiss tail. Red line shows fitting by a narrow-band–small-gap model (see text). Fitting parameters are listed. (b) Contribution to heat capacity from spin transition calculated by parameters obtained from magnetic susceptibility.

parameters obtained from the magnetization fit, we have calculated the spin state transition contribution to specific heat of $C_P = (\partial U/\partial T)$, with U given by the contribution from the valence and conduction bands:

$$U = \int_0^W \frac{Np}{W} \frac{EdE}{\exp[\beta(E - W - \Delta)] + 1} + \int_{W+2\Delta}^{2W+2\Delta} \frac{Np}{W} \frac{EdE}{\exp[\beta(E - W - \Delta)] + 1}. \quad (6)$$

The calculated heat capacity [Fig. 4(b)] shows a clear Schottky peak around 30 K, which is expected for a two-level electronic system separated by a narrow gap; however, the phonon contribution is dominant in the measured temperature range [Figs. 1(f) and 4(b)]; i.e., the phonon heat capacity dwarfs the Schottky peak contribution. We note that the difference between low-temperature energy gaps extracted from $\rho(T)$ and $\chi(T)$ could be explained by invoking the existence of the smallest indirect energy gap relevant for low-temperature transport, but not for χ [39]. Hence, magnetic properties indicate that the giant increase in low-temperature thermopower comes from the Kondo-insulatorlike low-temperature distortion in the density of the electronic states [40]. This is further supported by the rather low carrier mobility [Fig. 2(d)], which is comparable to values found in rare earth hybridization compounds and FeSi [41,42]. The low mobility of carriers implies a high effective band mass and calls for detailed photoemission studies.

In mixed anion compounds FeSbP and FeAsP related to $FeSb_2$, the size of the band gap is related to a rotation angle θ of the Fe-centered octahedron around the z axis [14]. Because the $Co(Sb, S)_6$ octahedra exhibit relatively large rotation displacements when compared to $Fe(Sb, P/As)_6$ due to corner sharing, a larger intrinsic band gap could be favored by the local crystallographic arrangement. The thermal conductivity of CoSbS is large, and electrical conductivity is much too low for a competitive thermoelectric material. However, because the transition metal character dominates near the band edge in density functional theory (DFT) calculations, alloying on the Sb or S atomic site may improve electrical conductivity; and it may be more effective in thermal conductivity reduction when compared to bulk nanostructuring methods due to very low sound velocity anisotropy [17].

Summary.—We have evaluated the low-temperature thermoelectric properties of CoSbS: a material that shows high thermoelectric performance above room temperature. Here, we show that CoSbS single crystals also exhibit giant thermopower at cryogenic temperatures. The mechanism of thermopower enhancement involves buildup of the electronic correlations on cooling; consequently, giant thermopower could be explained within the model of diffusive correlated electrons. Our work calls for further investigation of the Kondo-insulatorlike electronic correlations that develop at low temperature and for the relation of the diffusive thermopower to the 0.50 meV gap absent in DFT calculations [17]. The question of how giant diffusion thermopower in CoSbS is related to electronic structure and impurity states is an interesting subject for future study.

*petrovic@bnl.gov
†qdu@bnl.gov

[1] G. Jeffrey Snyder and Eric S. Toberer, Nat. Mater. 7, 105 (2008).
[2] J. He, M. G. Kanatzidis, and V. P. Dravid, Mater. Today 16, 166 (2013).
[3] G. Palsson and G. Kotliar, Phys. Rev. Lett. 80, 4775 (1998).
[4] W. Koshibae and S. Maekawa, Phys. Rev. Lett. 87, 236603 (2001).
[5] C. Petrovic, J. W. Kim, S. L. Budko, A. I. Goldman, P. C. Canfield, W. Choe, and G. J. Miller, Phys. Rev. B 67, 155205 (2003).
[6] C. Petrovic, Y. Lee, T. Vogt, N. Dj. Lazarov, S. L. Bud'ko, and P. C. Canfield, Phys. Rev. B 72, 045103 (2005).
[7] A. Bentien, S. Johnsen, G. K. H. Madsen, B. B. Iversen, and F. Steglich, Europhys. Lett. 80, 17008 (2007).
[8] Q. Jie, R. Hu, E. Bozin, A. Llobet, I. Zaliznyak, C. Petrovic, and Q. Li, Phys. Rev. B 86, 115121 (2012).
[9] M. Cutler and N. F. Mott, Phys. Rev. 181, 1336 (1969).
[10] H. Fritzche, Solid State Commun. 9, 1813 (1971).
[11] P. Sun, N. Oeschler, S. Johnsen, B. B. Iversen, and F. Steglich, Phys. Rev. B 79, 153308 (2009).
[12] P. Sun, W. Xu, J. M. Tomczak, G. Kotliar, M. Sondergaard, B. B. Iversen, and F. Steglich, Phys. Rev. B 88, 245203 (2013).
[13] H. Takahashi, R. Okazaki, S. Ishiwata, H. Taniguchi, A. Okutani, M. Hagiwara, and I. Terasaki, Nat. Commun. 7, 12732 (2016).
[14] C.-J. Kang and G. Kotliar, Phys. Rev. Mater. 2, 034604 (2018).
[15] H. Nahigian, J. Steger, H. L. McKinzie, R. J. Arnott, and A. Wold, Inorg. Chem. 13, 1498 (1974).
[16] R. Carlini, C. Artini, G. Borzone, R. Masini, G. Zanicchi, and G. A. Costa, J. Therm. Anal. Calorim. 103, 23 (2011).
[17] D. Parker, A. F. May, H. Wang, M. A. McGuire, B. C. Sales, and D. J. Singh, Phys. Rev. B 87, 045205 (2013).
[18] Z. Liu, H. Geng, J. Shuai, Z. Wang, J. Mao, D. Wang, Q. Jie, W. Cai, J. Sui, and Z. Ren, J. Mater. Chem. C 3, 10442 (2015).
[19] R. Chmielowski, S. Bhattacharya, S. Jacob, D. Pere, A. Jacob, K. Moriya, B. Delatouche, P. Roussel, G. Madsen, and G. Dennler, Sci. Rep. 7, 46630 (2017).

[20] R. Chmielowski, S. Bhattacharya, W. Xie, D. Pere, S. Jacob, R. Stern, K. Moriya, A. Weidenkaff, G. K. H. Madsen, and G. Dennler, J. Mater. Chem. **4,** 3094 (2016).

[21] S. Bhattacharya, R. Chmielowski, G. Dennlerb, and G. K. H. Madsena, J. Mater. Chem. **4,** 11086 (2016).

[22] V. Jaccrino, G. K. Wertheim, J. H. Wernick, L. R. Walker, and S. Arajs, Phys. Rev. **160,** 476 (1967).

[23] D. Mandrus, J. L. Sarrao, A. Migliori, J. D. Thompson, and Z. Fisk, Phys. Rev. **51,** 4763 (1995).

[24] D. A. Neamen, *Semiconductor Physics and Devices, Basic Principles* (McGraw-Hill, New York, 1992).

[25] F. Hulliger and E. Mooser, J. Phys. Chem. Solids **26,** 429 (1965).

[26] Z. Schlesinger, Z. Fisk, H.-T. Zhang, M. B. Maple, J. F. DiTusa, and G. Aeppli, Phys. Rev. Lett. **71,** 1748 (1993).

[27] Orson L. Anderson, J. Phys. Chem. Solids **24,** 909 (1963).

[28] J. S. Kim, J. Appl. Phys. **86,** 3187 (1999).

[29] Y. Hadano, S. Narazu, M. A. Avila, T. Onimaru, and T. Takabatake, J. Phys. Soc. Jpn. **78,** 013702 (2009).

[30] T. Pietrus, H. V. Löhneysen, and P. Schlottmann, Phys. Rev. B **77,** 115134 (2008).

[31] K. Behnia, D. Jaccard, and J. Floquet, J. Phys. Condens. Matter **16,** 5187 (2004).

[32] N. Tsujii, A. Nishide, J. Hayakawa, and T. Mori, Sci. Adv. **5,** eaat5935 (2019).

[33] O. Mentré, Y. Kanke, A-C. Dhaussy, P. Conflant, Y. Hata, and E. Kita, Phys. Rev. B **64,** 174404 (2001).

[34] J. Callaway, Phys. Rev. **113,** 1046 (1959).

[35] Conyers Herring, Phys. Rev. **96,** 1163 (1954).

[36] L. Weber and E. Gmelin, Appl. Phys. A **53,** 136 (1991).

[37] H. J. Goldsmid, *Introduction to Thermoelectricity*, Springer Series in Materials Science Vol. 121 (Springer, New York, 2016).

[38] L. H. Nguyen, H. Riegel, M. Asen-Palmer, and E. Gmelin, Physica (Amsterdam) **218B,** 248 (1996).

[39] S. Paschen, E. Felder, M. A. Chernikov, L. Degiorgi, H. Schwer, H. R. Ott, D. P. Young, J. L. Sarrao, and Z. Fisk, Phys. Rev. B **56,** 12916 (1997).

[40] J. P. Heremans, B. Wiendlocha, and A. M. Chamoire, Energy Environ. Sci. **5,** 5510 (2012).

[41] B. C. Sales, E. C. Jones, B. C. Chakoumakos, J. A. Fernandez-Baca, H. E. Harmon, J. W. Sharp, and E. H. Volckmann, Phys. Rev. B **50,** 8207 (1994).

[42] Z. Fisk, P. C. Canfield, J. D. Thompson, and M. F. Hundley, J. Alloys Compd. **181,** 369 (1992).